Electronic Supporting Information

Uncovering the microscopic mechanism of incorporating Mn^{2+} ions into $CsPbCl_3$ crystal lattice

Jienan Xia,[a,†] Song Lu,[b,†] Lei Lei,[a*] Youjie Hua,[a] Shiqing Xu[a*]

[a]Institute of Optoelectronic Materials and Devices, China Jiliang University, Hangzhou 310018, P R. China

[b]Department of Physical and Macromolecular Chemistry, Faculty of Science, Charles University in Prague, 128 43 Prague 2, Czech Republic

[†] These authors contributed equally to this work.

Characterizations. The crystal structures were tested by X-ray diffraction (XRD), using a powder diffractometer (Bruker D8 Advance), with a radiation of Cu-Kα (λ= 1.5405 Å). The morphology of the products was characterized by scanning transmission electron microscopy (STEM) using a field emission transmission electron microscope (TEM, FEI Tecnai G^2 F20). All the samples were prepared through diluting the nanocrystals in cyclohexane, then dropping it onto a copper grid coated with carbon film and evaporating the solvent afterwards. X-ray photoelectron spectroscopy (XPS) analysis was carried out using a 250Xi ESCA system under Al Kα irradiation. All the binding energies were calibrated to the C 1s peak of the surface adventitious carbon at 284.6 eV. The actual chemical compositions were measured via the inductively coupled plasma (ICP) technique with a PerkinElmer Optima 3300DV spectrometer. Optical absorption (Abs.) spectra were measured by using a UV-VIS-NIR spectrophotometer (Shimadzu UV3600). Photoluminescence (PL), photoluminescence excitation (PLE), photoluminescence quantum yield (PLQY) and Mn^{2+} decay curves for the Mn-doped $CsPbCl_3$ NCs were performed by an Edinburgh Instruments FLS920 spectrophotometer using Xenon lamps as the excitation source. The temperature dependent photoluminescence properties were recorded by the above spectrometer equipped with a TAP-02 temperature controller (ORIENT KOJI, China).

Computation method (Part Ⅱ).

Considering the chemical potentials of constitute elements could make a big difference to the defect formation energies[1], we calculated the stability region of different products against Pb and Cl chemical potential. First, the chemical potentials of Cs, Pb and Cl atoms should be less than 0 eV, so as to avoid the formation of those elementary substances during the synthetic process. Besides, equilibrium growth of a stable $CsPbCl_3$ also required the chemical potentials satisfy that[2]

$$\mu(\mathrm{Cs}) + \mu(\mathrm{Pb}) + \mu(\mathrm{Cl}) = \Delta E(\mathrm{CsPbCl_3}) = -17.625 \text{ eV}$$

where $\Delta E(CsPbCl_3)$ was the total energy of the pristine $CsPbCl_3$ single cell. Finally, in order to avoid the formation of secondary products such as CsCl and $PbCl_2$, we set up the following restrictions,

$$\mu(\mathrm{Cs}) + \mu(\mathrm{Cl}) \ < \Delta E\ (\mathrm{CsCl}) = -6.101 \text{ eV}$$

$$\mu(\mathrm{Pb}) + 2\mu(\mathrm{Cl}) \ < \Delta E\ (\mathrm{PbCl_2}) = -10.705 \text{ eV}$$

where $\Delta E(CsCl)$ and $\Delta E(PbCl_2)$ were the total energies of the CsCl and $PbCl_2$ single cells, respectively. Under all the above limitations, the available equilibrium chemical potential region for $CsPbCl_3$ was achieved (Figure 4a).

In this work, we considered several point defects (V_{Pb}, V_{Cl}, $V_{Pb\text{-}Cl}$ and $V_{Pb\text{-}2Cl}$) in the pristine $CsPbCl_3$. The $V_{Pb\text{-}Cl\text{-}1}$, $V_{Pb\text{-}Cl\text{-}2}$ and $V_{Pb\text{-}Cl\text{-}3}$ were three differnt $V_{Pb\text{-}Cl}$ double vancaies (Figure S1, ESI), where $V_{Pb\text{-}Cl\text{-}1}$ represented bond [Pb---Cl] vacancy pair, $V_{Pb\text{-}Cl\text{-}2}$ represneted a Pb^{2+} vacancy together with a non-connective but closer Cl^- vancany and $V_{Pb\text{-}Cl\text{-}3}$ represneted a Pb^{2+} vacancy together with a non-connective and farther distance Cl^- vancany. Two characteristic points A and B shown in Figure 4a which represneted different growth environment were chosen to calculate the formation energies of kinds of defective crystals. Furthermore, the total charge density of (0 0 1) surface of pristine and Mn-doped $CsPbCl_3$ were calculated to reveal the size evolution mechanism.

Table S1. The formation energies of diverse defects in $CsPbCl_3$ at Points A and B (Figure 4a) with unit eV. V_{Pb} and V_{Cl} represented single Pb^{2+} or Cl^- vacancy, $V_{Pb\text{-}Cl\text{-}1}$, $V_{Pb\text{-}Cl\text{-}2}$ and $V_{Pb\text{-}Cl\text{-}3}$ were three types of double vacancies, which were illustrated in Figure S1. $D_{Mn\text{-}Cl}$ and D_{Mn} were the respectively introducing of the [Mn---Cl] ion pair and Mn^{2+} into the Pb^{2+}-vacancy involved defective crystal structure with the lowerst FE. Sub_{Mn} represented the substitution energy of repalcing Pb^{2+} ions by Mn^{2+} ions in a perfect crystal structure.

	V_{Cl}	V_{Pb}	$V_{Pb\text{-}Cl\text{-}1}$	$V_{Pb\text{-}Cl\text{-}2}$	$V_{Pb\text{-}Cl\text{-}3}$	$D_{Mn\text{-}Cl}$	D_{Mn}	Sub_{Mn}
Cl-rich	3.618	1.451	1.364	2.130	2.254	**-1.151**	2.334eV	0.213
Cl-poor	0.918	5.913	3.126	3.892	4.016	1.549		4.675

Table S2. Mn^{2+} doping contents determined from inductively coupled plasma atomic emission spectroscopy (ICP-AES).

Cs: Pb: Cl: Mn precursors ratio	Mn^{2+} doping content from ICP-AES (mol%)
1:1:3-1	2.51
1:1:4.5-1	5.65
1:1:6-1	8.12

Figure S1-S9

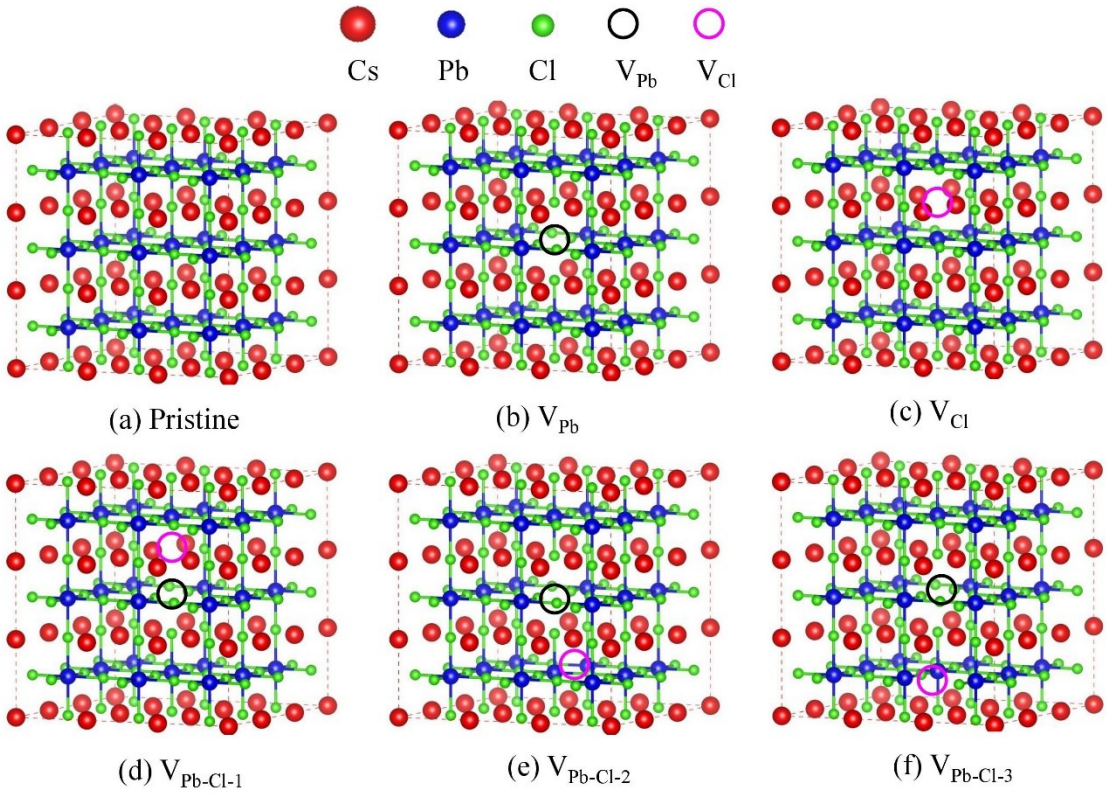

Figure S1. Crystal structure of (a) pristine, (b) Pb^{2+} vacancy V_{Pb}, (c) Cl^- vacancy V_{Cl}, (d) Pb^{2+} vacancy bond with Cl^- vacancy $V_{Pb\text{-}Cl\text{-}1}$, (e) Pb^{2+} vacancy together with non-connective but closer Cl^- vacancy $V_{Pb\text{-}Cl\text{-}2}$, (f) Pb^{2+} vacancy together with non-connective but farther Cl^- vacancy $V_{Pb\text{-}Cl\text{-}3}$.

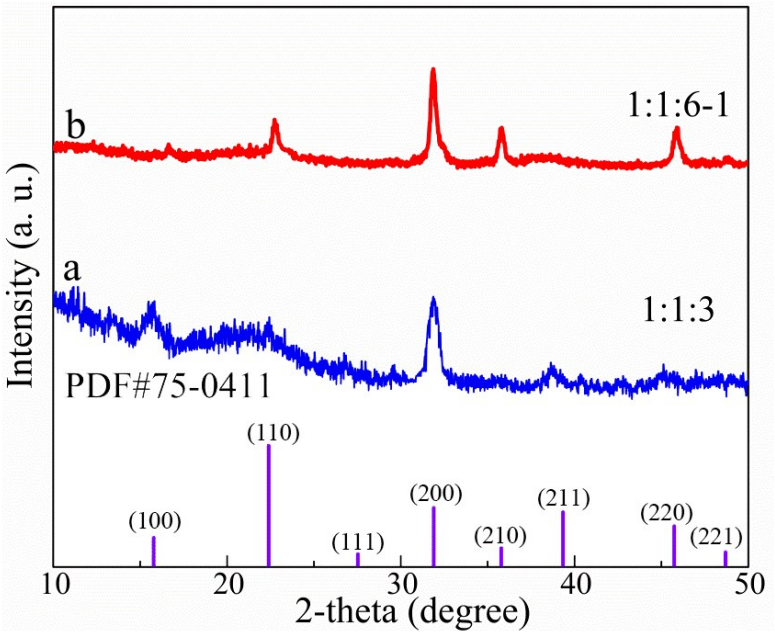

Figure S2. XRD patterns of the as-prepared $CsPbCl_3$ nanocrystals at a stoichiometry precursors content and Mn^{2+} doped $CsPbCl_3$ QDs at excesscive Cl^- content.

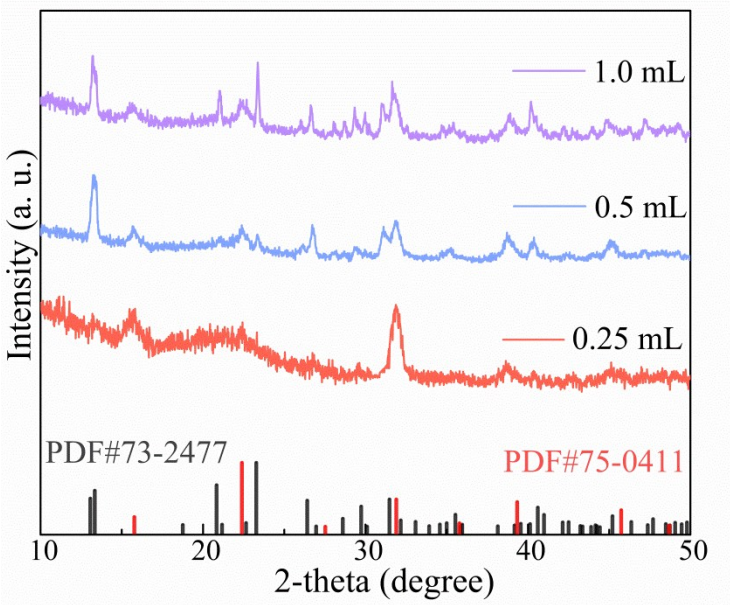

Figure S3. XRD patterns of the $CsPbCl_3$ nanocrystals prepared with different acetone content.

Acetone could promote the ionization of the precursors including CsOOR (cerium oleate complex) and $Pb(OOR)_2$ (lead oleate complex), and then nucleation of $CsPbCl_3$. Equations of the ionization equilibrium of the precursors and the subsequent nucleation processes were given as below:

$$CsOOR \leftrightarrow Cs^{+} + ROO^{-} \quad (1)$$

$$Pb(OOR)_2 \leftrightarrow Pb^{2+} + 2ROO^{-} \quad (2)$$

$$RNH_3Cl \leftrightarrow RNH_3^{+} + Cl^{-} \quad (3)$$

$$Cs^{+} + Pb^{2+} + 3Cl^{-} \leftrightarrow CsPbCl_3 \quad (4)$$

$$4Cs^{+} + Pb^{2+} + 6Cl^{-} \leftrightarrow Cs_4PbCl_6 \quad (5)$$

As a result, only $CsPbCl_3$ phase was formed below a critical Cs^{+}, Pb^{2+} and Cl^{-} concentration. With the increase of acetone, the greatly enhanced ionization rate resulted a high concentration of Cs^{+}, Pb^{2+} and Cl^{-} ions in the reaction solution, which then led to the formation of Cs_4PbCl_6 phase accompany with $CsPbCl_3$ phase.

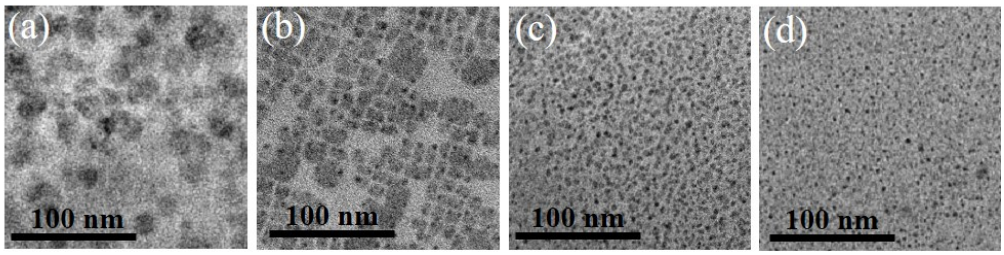

Figure S4. TEM images of the $CsPbCl_3$: Mn nanocrystals under the condition of different Cl^- contents: (a) 1.5 mM, (b) 3 mM, (c) 4.5 mM and (d) 6 mM.

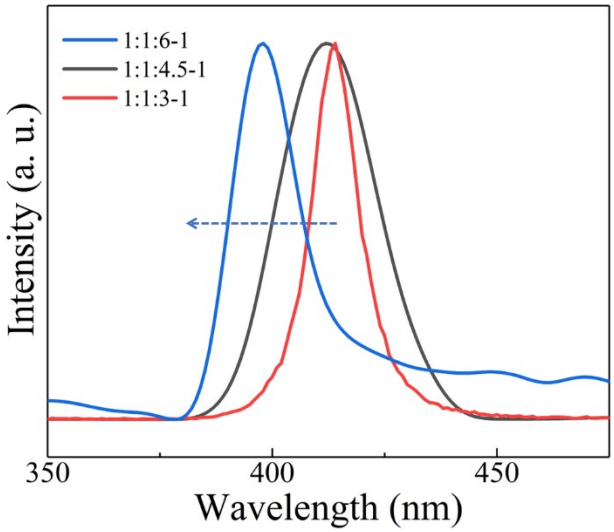

Figure S5. PL spectra of the Mn^{2+} doped $CsPbCl_3$ perovskites under the condition of different Cl^- content.

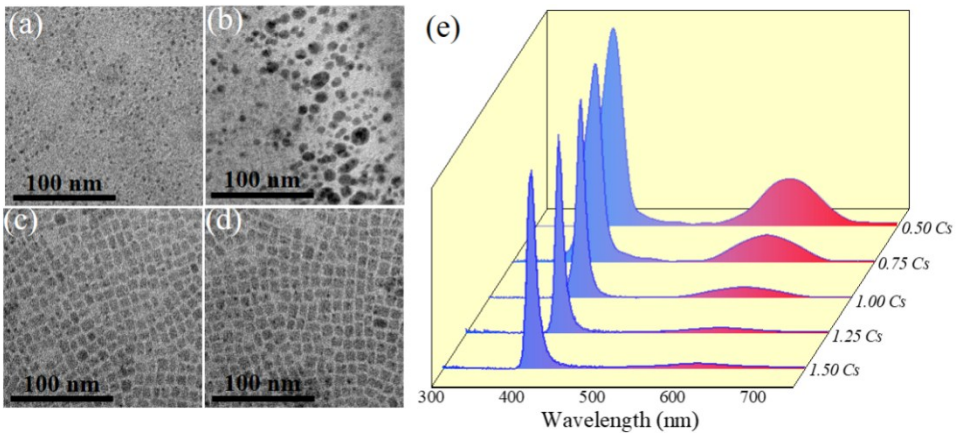

Figure S6. TEM images of the $CsPbCl_3$: Mn nanocrystals under the condition of different Cs^+ contents: (a) 0.50 mM, (b) 0.75 mM, (c) 1.25 mM and (d) 1.5 mM. (e) PL spectra at different Cs^+ contents.

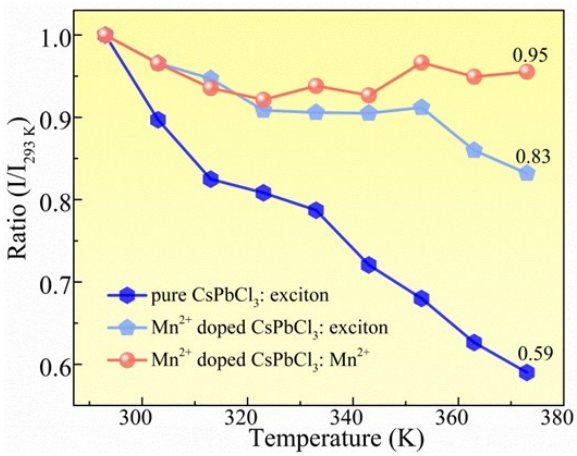

Figure S7. Temperature dependent integral emission intensities of pure $CsPbCl_3$, Mn^{2+} and exciton in the Mn^{2+} doped $CsPbCl_3$ QDs.

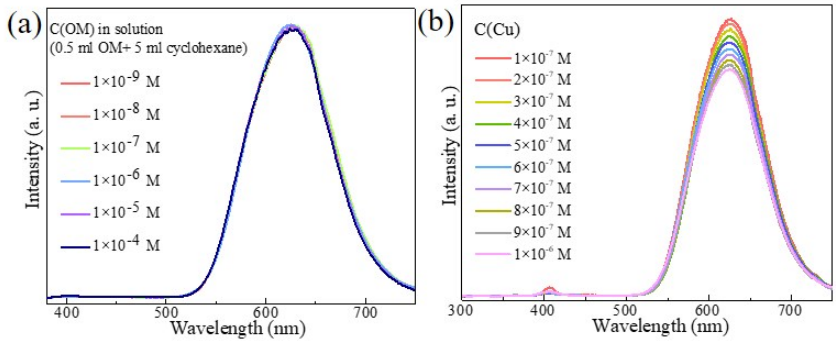

Figure S8. (a) PL spectra of the $CsPbCl_3$: Mn suspensions at different OM concentration. (b) PL spectra of the $CsPbCl_3$ suspensions versus Cu^{2+} concentration ranging from 1×10^{-7} M to 1×10^{-6} M.

The relationship between I/I_0 and concentration of Cu^{2+} ion could be fitted well by the following equation:

$$I/I_0 = A + K[C] \qquad (1)$$

Where I and I_0 were the PL intensities with and without Cu^{2+} ions, respectively. A was the fitted intercept, K was the slope (sensitivity), and [C] represented the concentration of Cu^{2+} ions. As shown in Figure 5d, the relationship was linearly fitted well with R^2=0.999. Thus, the limit of detection (LOD) was calculated, basing on the equation of

$$LOD = 3\sigma/K \qquad (2)$$

Where σ was the standard deviation of the blank.

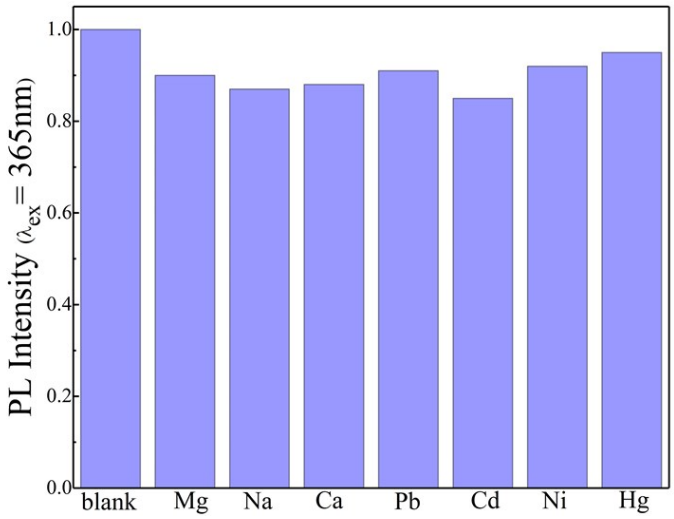

Figure S9. Mn^{2+} PL intensity (I) under different metal ions. The metal ions concentration was 1.0×10^{-3} M.

References

[1] J. Kang and L. Wang, *J. Phys. Chem. Lett.,* **2017**, 8, 489−493.

[2] Z. Yong, S. Guo, J. Ma, J. Zhang, Z. Li, Y. Chen, B. Zhang, Y. Zhou, J. Shu, J. Gu, L. Zheng, O. M. Bakr and H. T. Sun, *J. Am. Chem. Soc.,* **2018**, 140, 9942-9951.